Supplementary Information (SI) for Energy & Environmental Science.

Supporting information

Compacting surface charge Layer for efficient charge transfer toward stable Zn anode

Sinan Zheng[1,2], Yang Wang[1,2,*], Bin Luo[1,2], Kun Zhang[2], Leilei Sun[1,2], Zhean Bao[1,2], Guosheng Duan[1,2], Dinghao Chen[1,2], Hanwei Hu[1,2], Jingyun Huang[1,2,3,*] and Zhizhen Ye[1,2,*]

[1]School of Materials Science and Engineering, State Key Laboratory of Silicon and Advanced Semiconductor Materials, Zhejiang University, Hangzhou 310027, Zhejiang, China

[2]Institute of Wenzhou, Zhejiang University, Wenzhou 325006, Zhejiang, China

[3] Longmen Laboratory, Luoyang 471000, China

*Corresponding author

E-mail: wangy_zju@zju.edu.cn, huangjy@zju.edu.cn, yezz@zju.edu.cn

Keywords: Charge transfer, compressed EDL, ion distribution, aqueous Zn-ion batteries

Experiment Section

Electrolyte preparation

Zinc sulfate heptahydrate ($ZnSO_4 \cdot 7H_2O$, 99.9%) were supplied by Aladdin. 2M $ZnSO_4$ aqueous electrolyte is prepared using $ZnSO_4 \cdot 7H_2O$ and deionized water based on the molar ratio. Different amounts Metformin hydrochloride (MF·HCl, Aladdin, 99%) additives (i.e., 5 mM, 10 mM, 20 mM, 40 mM) were introduced into the $ZnSO_4$ electrolyte. The $ZnSO_4$+MF·HCl shown in the Figures refer to the optimal concentration of MF·HCl added in the $ZnSO_4$ electrolyte (i.e., 20 mM).

Preparation of electrodes and cells:

The Zn||Zn symmetric cells, Cu||Zn asymmetric cells were assembled in CR2016 coin cell configurations. The preparation of $NaV_3O_8 \cdot 1.5H_2O$ (NVO)was based on the previous research reported by Chen's group. Typically, 1 g commercial V_2O_5 powder was dissolved into 15 ml 2 M NaCl aqueous solution. After that, put the mixed solution into water bath at 30 °C for 96 hours under the condition of stirring. Ultimately the black red powder was obtained by washing and freeze-drying. The slurry mixed with NVO powder, carbon black and polyvinylidene fluoride (PVDF) binder with a mixing weight proportion of 7:2:1 in N-methyl-2-pyrrolidone (NMP) were coated on carbon paper for vacuum-drying at 90 °C of 12 h to prepare NVO cathode. The active loading mass of NVO electrodes were ~7.35 mg cm^{-2} and ~9.25 mg cm^{-2}. The Zn electrodes (20 μm) were used to assemble full cells for N/P ratio of 3:1.

All the anode and cathode were cut into circular discs with a diameter of 11.3 mm (1 cm^2). The electrolyte applied in Zn||Zn symmetric cell, Cu||Zn asymmetric cell and Zn||NVO full cell was 2 M $ZnSO_4$ aqueous solution. The discharge/charge tests of all cell configurations are carried out on Neware CT-4008 batteries testing system. For the Cu||Zn asymmetric cell, the charging cut-off voltage was set as 0.5 V. The voltage window for Zn||NVO full cell was at 0.4-1.5 V versus Zn/Zn^{2+}.

Material characterization：

The X-ray diffraction (XRD) patterns were recorded on a Rigaku Smart Lab SE X-ray diffractometer with Cu K_α radiation (40 kV, 30 mA). Scanning electron microscopy

(SEM, Zeiss) images were employed to display micromorphology of Zn cycled in $ZnSO_4$ and $ZnSO_4$+MF·HCl electrolyte at different current densities. X-ray photoelectron spectroscopy (XPS) analysis was carried out on a Thermo Scientific K-Alpha. XPS test samples are Zn foils after cycling that have been treated as follows: first, the surface of the foils removed from cycled cells was washes with deionized water, then the membrane on the surface of Zn foils was removed by sonication for 10s in a Petri dish containing alcohol and finally dries naturally. And the samples were not subjected to any secondary treatment before the XPS test. In-situ SO_4^{2-} changes during discharge process were monitored by high-resolution confocal Raman (Horiba LabRAM HR Evolution) with a 532 nm laser. The surface potential of immersed Zn was measured to analyze surface charge distribution using the KPFM mode of AFM platform using Bruker Dimension Icon. Fourier transforms infrared (FTIR) spectra were recorded on Thermo Scientific Nicolet iS20 in the wavenumber range of 400-4000 cm^{-1}. NMR spectra were carried out by the machine with the instrument model of Bruker AVANCE NEO 400M. Laser Spectroscopy images (KEYENCE VK-X150) were used to verify the effect of MF·HCl additive on surface homogeneity of Zn electroplating and corrosion state.

Electrochemical measurements:

Cyclic voltammetry (CV) and chronoamperometry (CA) measurements were carried out on an electrochemical workstation (Chenhua, CHI760E, shanghai). The double layer capacitance was proved by differential capacitance (DC) using 1 M Na_2SO_4 as basic electrolyte and CV of symmetric cells at different sweep speeds in the range of non-Faraday current. The DC technique was performed using Zn||Ti half cells from 0 V to 0.45 V, with amplitude of 0.05 V and frequency of 1000 Hz. CV technology was carried out for the nucleation overpotential (NOP) on the electrochemical workstation using Zn||Ti half cells at the voltage range from -0.2-0.4 V with a scan speed of 1 mV s^{-1}. The diffusion mode curves were measured by CA method under a bias voltage of 150 mV over 300s using symmetrical cell. The electrochemical window of electrolytes implemented by Linear sweep voltammetry (LSV) was measured at a voltage range of 0.3 V to -0.5 V in negative sweep direction for hydrogen evolution reaction (HER) at a scan rate of 1 mV s^{-1}. Tafel plots were conducted in a three-electrode method. Zn foils were used as the working electrode, the Pt plate as the counter electrode, and the calomel electrode as the reference electrode. The EIS spectra were recorded on the electrochemical workstation with a frequency range from 100 kHz to 0.1 Hz. EQCM tests were carried out using an eQCM 10M quartz crystal analyzer (Gamry Instruments, America). EQCM was performed under CV testing using a three-electrode system with coated Zn on Au quartz crystal as the working electrode, Pt wire as the counter electrode, Ag/AgCl as the reference electrode, and 1 M Na_2SO_4 with or without MF·HCl as the electrolyte. The Na_2SO_4 electrolyte was intentionally Zn^{2+}-free to isolate the mass response of MF^{2+} adsorption, excluding Zn-related contributions.

Computational methods

1. Molecular Dynamics (MD) Simulations

Quantum chemistry calculations were first performed to optimize molecular geometries of MF·HCl molecule and SO_4^{2-} using the Gaussian 16 package[1] at B3LYP/6-311g(d,p) level of theory. The partial charge of SO_4^{2-} ions were calculated using Gaussian 16 code and the 6-311g (d,p) basis functions were applied. The atomistic force field parameters for all ions and molecules are described by the OPLS-AA.[2] And Zn atom is described by the UFF. The SPC/E water model was adopted in the current work.

Atomistic simulations were performed using GROMACS package with cubic periodic boundary conditions [1]. The equations for the motion of all atoms were integrated using a classic Verlet leapfrog integration algorithm with a time step of 2.0 fs. A cutoff radius of 1.4 nm was set for short-range van der Waals interactions and real-space electrostatic interactions. The particle-mesh Ewald (PME) summation method with an interpolation order of 4 and a Fourier grid spacing of 0.12 nm was employed to handle long range electrostatic interactions in reciprocal space. In all the three directions, periodic boundary conditions were imposed. Leapfrog algorithm was used to integrate the Newtonian equation of motion.[2] The MD simulation was processed in an NVT ensemble and the simulation time is 20 ns and the temperature was maintained by the V-rescale thermostat at 298.15 K.

To characterize the local structures surrounding Zn^{2+} in the electrolytes, the radial distribution function with reference to Zn^{2+} was calculated

$$g(r) = \frac{n_r}{4\pi r^2 \rho \Delta r} \tag{3}$$

where r is the distance of a species from the referenced Zn^{2+} ion, ρ is the average probability density of the Zn^{2+} ions in the electrolyte, and n_r is the number of interested species particles within a shell of thickness Δr. By integrating the $g(r)$ with respect to r, one can obtain the coordination number (CN) of Zn^{2+} ion with the neighbour species

$$\mathrm{CN} = \int_0^r 4\pi r^2 \rho g(r) \tag{4}$$

If the upper limit of the integral is taken to be the first minimum of $g(r)$, the CN gives the information of the first solvation shell.

2. DFT calculations

To conduct all density functional theory (DFT) computations within the generalized gradient approximation (GGA) framework, we utilized the Vienna Ab Initio Simulation Package (VASP),[3] employing the Perdew-Burke-Ernzerhof (PBE) functional.[4] The ionic cores were represented using projected augmented wave (PAW) potentials, while the valence electrons were accounted for with a plane wave basis set, applying a kinetic energy cutoff of 450 eV.[5, 6] To accommodate partial occupancies of Kohn-Sham orbitals, we applied the Methfessel-Paxton method of order 1, with a smearing width of 0.2 eV. The electronic energy was deemed self-consistent when the energy change was less than 10−5 eV. Geometric optimization was considered complete when the force on each atom was less than 0.02 eV $Å^{-1}$. A vacuum layer of 18 Å was introduced perpendicular to the plane of the structure to minimize interactions between periodic images. All structural calculations were performed using a gamma-centered k-point mesh of 1 × 1 × 1. The DFT+D3 method, incorporating Grimme's empirical corrections,[7] was employed to describe weak interactions.

The adsorption energy (Eads) was calculated using the following equation:

$$\text{Eads} = E_{\text{total}} - E_{\text{substrate}} - E_{\text{adsorbate}}$$

Here, E_{total}, $E_{\text{substrate}}$, and $E_{\text{adsorbate}}$ represent the total energy of the adsorbed system, the substrate (Zn(002)), and the adsorbate (MF·HCl/H_2O molecule), respectively.

3. AIMD and Barder charge caculation

All calculations were carried out with CP2K package (version 7.1) in the framework of the density functional theory,[8] based on the hybrid Gaussian and plan-wave scheme.[9] Molecular orbitals of the valence electrons were expanded into DZVP-MOLOPT-SR-GTH basis sets,[4] and the exchange-correlation between the electrons were treated by employing the Predew-Burke-Ernzerhof (PBE) functional supplemented with the Grimmes D3 dispersion correction.[7] The interaction between the valence electrons and atomic cores were described by the norm-conserving Goedecker-Teter-Hutter (GTH) pseudopotentials.[10] A plane-wave density cutoff of 500 Ry was adopted. All the structures fully relaxed by CP2K with BFGS scheme, and the force convergence criterion was set to $4.5 * 10^{-4}$ hartree/bhor.

Before the static calculations, the microstructures of the interface between Zn(002) plane and the electrolyte were explored by AIMD calculations. The initial structures were prebuilt by PACKMOL code and pre-optimized in CP2K code. The AIMD simulations were performed at a constant temperature of 300 K using the Nosé-Hoover thermostat 11to ensure that the system reached equilibrium. The time step for the AIMD calculations was set to 1.0 fs, and the simulations were run for a total of 10 ps.

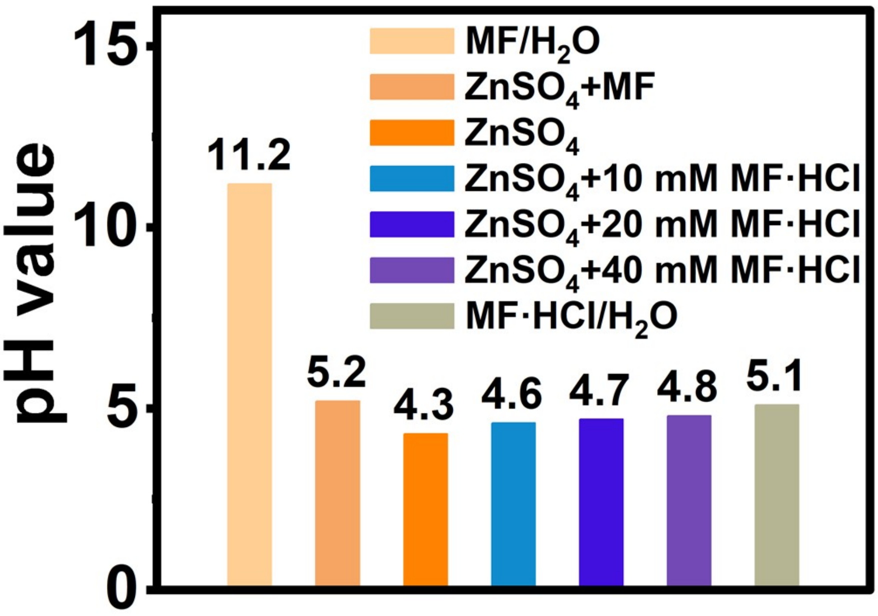

Figure S1. The pH value of $ZnSO_4$ solution with different additives.

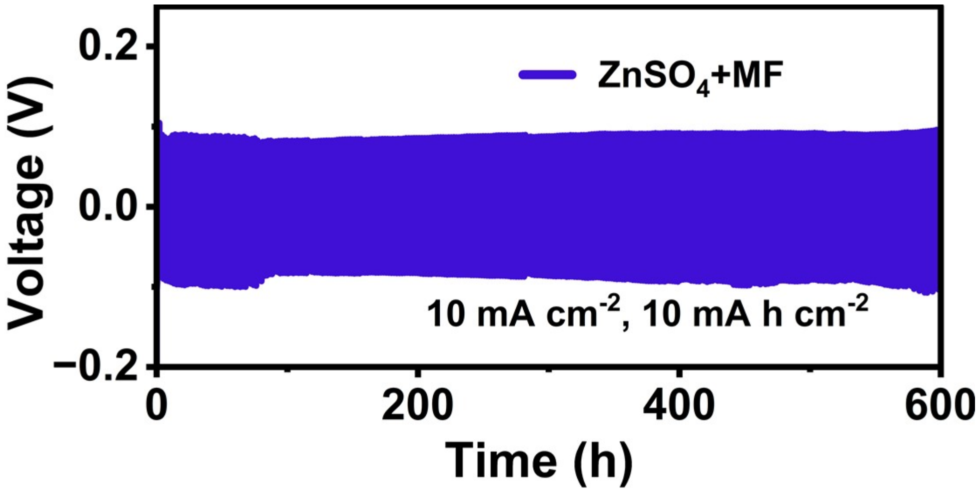

Figure S2. The performance of the symmetrical battery at 10 mA cm^{-2} and 10 mAh cm^{-2} under the addition of metformin additive (optimal amount)

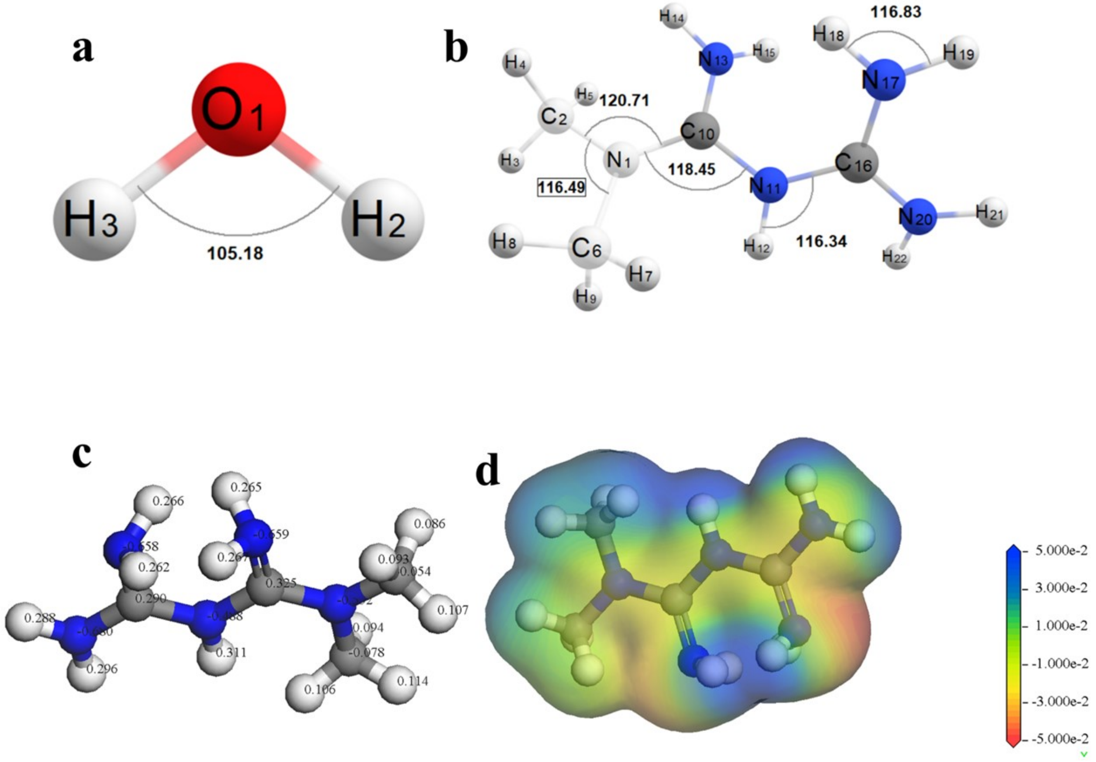

Figure S3. Molecular properties of water and additives. (a) Bond angle of water and (b) MF^{2+}. (c) The corresponding charge density of each atom of MF^{2+}. (d) Electrostatic potential distribution of MF^{2+}.

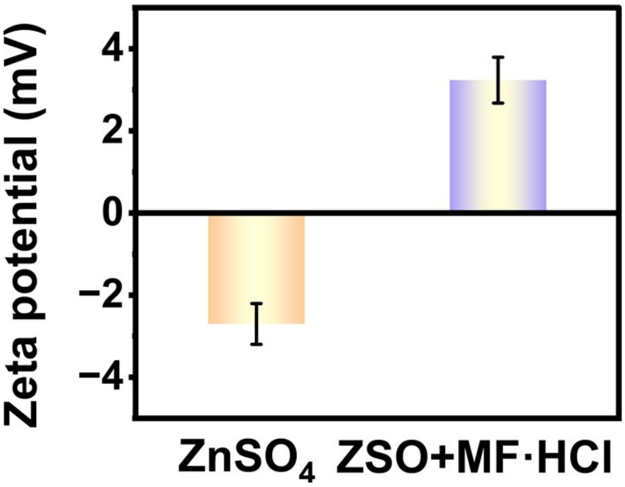

Figure S4. The Zeta potentials of $ZnSO_4$ and $ZnSO_4$+MF·HCl electrolytes.

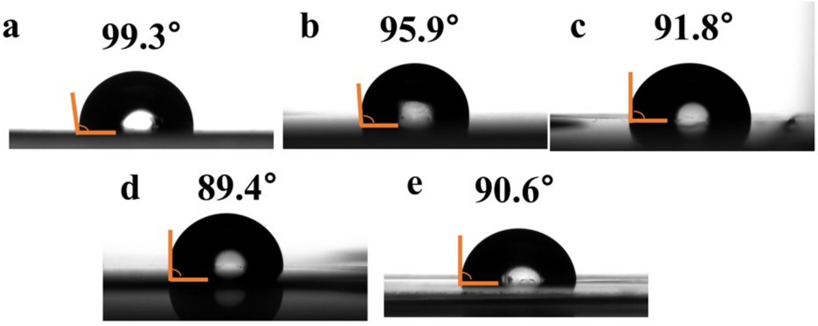

Figure S5. (a) The contact angle of $ZnSO_4$ electrolyte, (b) ZSO-5 mM MF·HCl, (c) ZSO-10 mM MF·HCl, (d) ZSO-20 mM MF·HCl and (e) ZSO-40 mM MF·HCl on an untreated Zn surface.

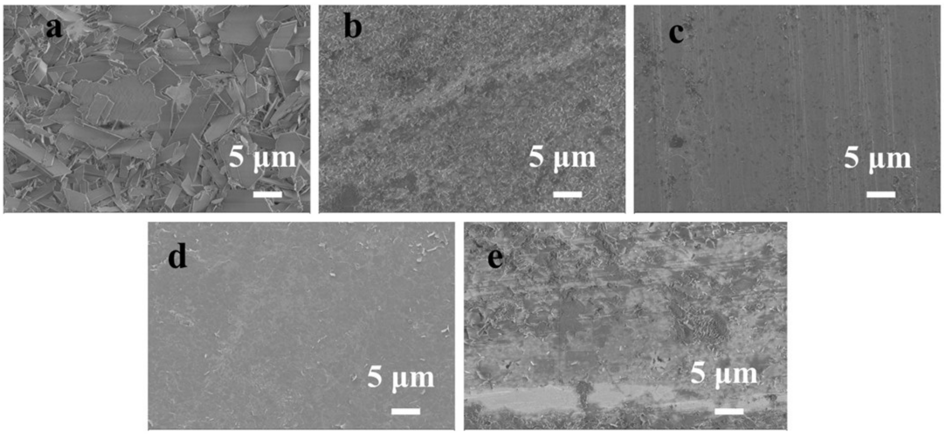

Figure S6. The morphology Zn foil immersed in electrolyte containing different concentrations of MF·HCl for 5 days (a: 0 mM, b: 5 mM, c:10 mM, d:20 mM, e: 40 mM).

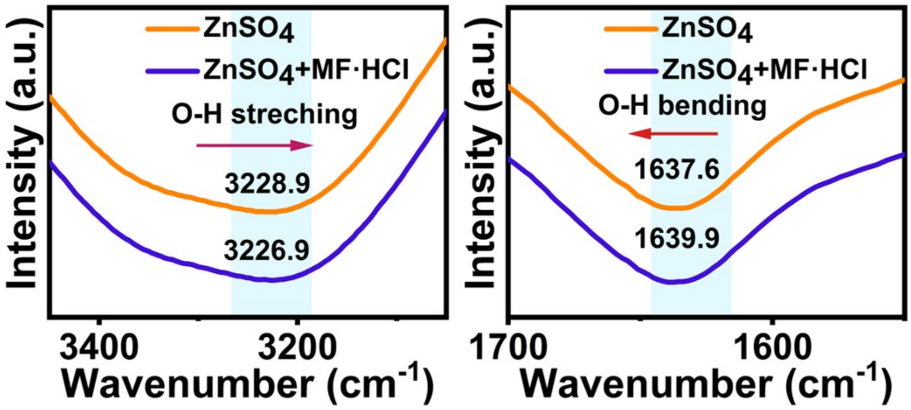

Figure S7. The FTIR spectra of two electrolytes for O-H peaks.

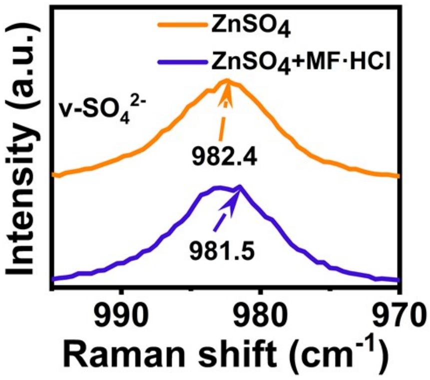

Figure S8. Raman spectra of $ZnSO_4$ and MF·HCl-contained electrolytes.

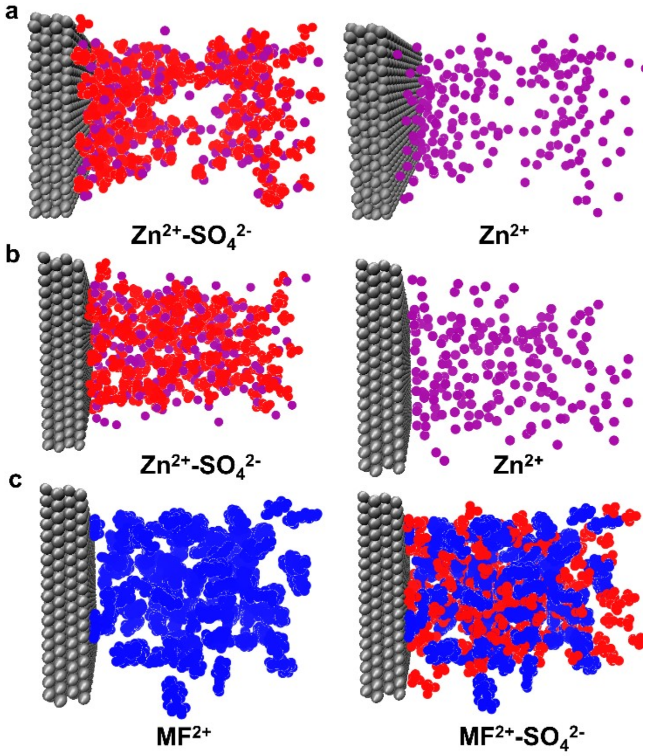

Figure S9. a) Distribution of Zn^{2+} and Zn^{2+}-SO_4^{2-} in $ZnSO_4$ system and b) MF·HCl-contained electrolyte. c) Distribution of MF and MF-SO_4^{2-} in the electrolyte in which MF·HCl is involved.

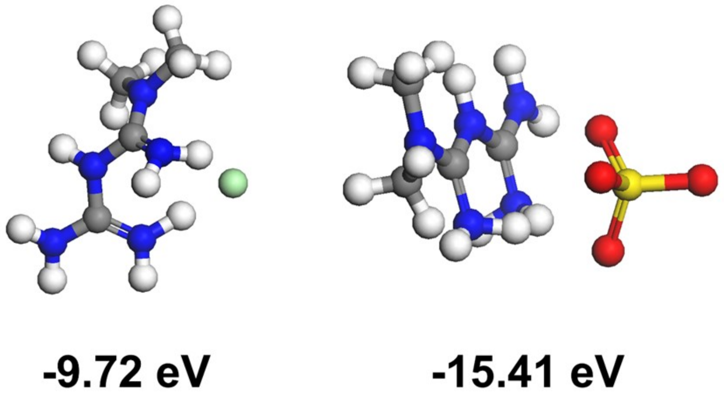

Figure S10. Binding energy of MF^{2+} with C^{l-} and $SO4^{2-}$.

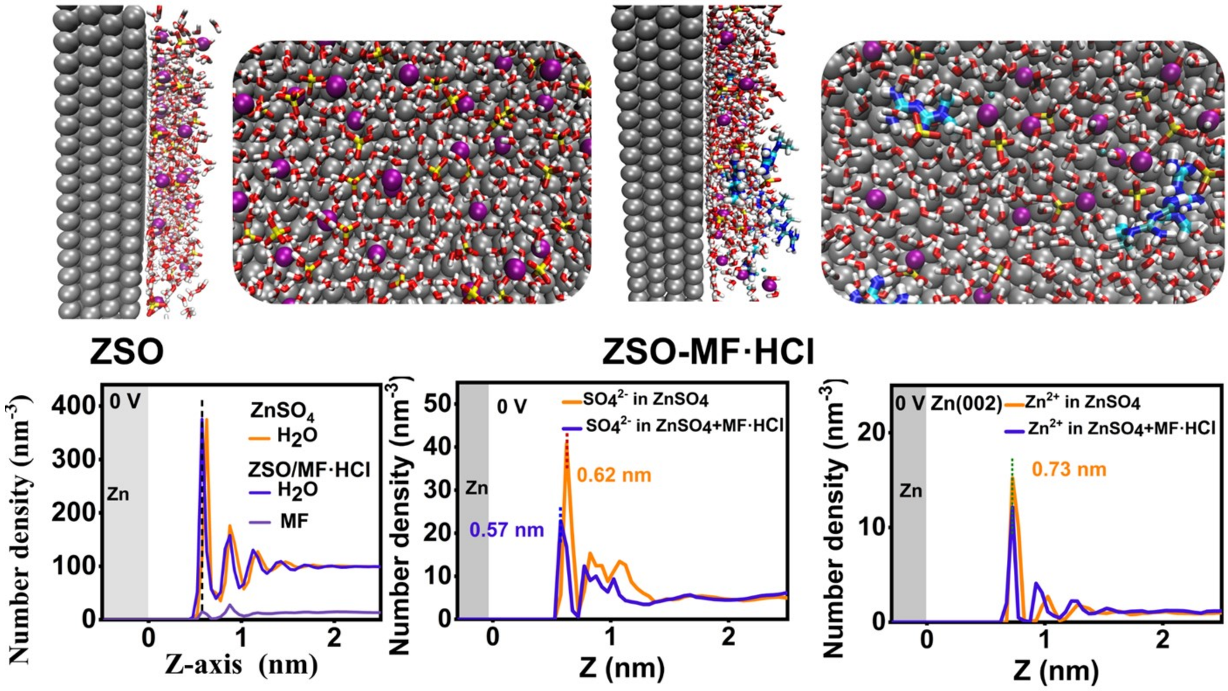

Figure S11. Snapshots of the EDL side and front of the two electrolytes at 0V and the quantity density of different ionic charges.

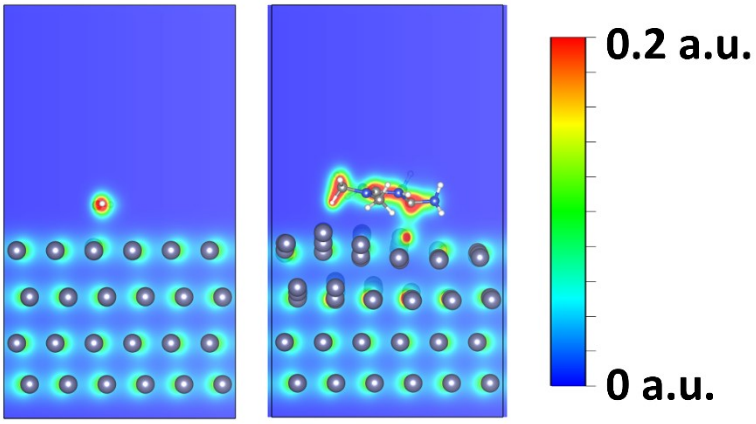

Figure S12. Adsorption configuration and electrostatic potential distribution of water and MF^{2+} on Zn (002) crystal surface

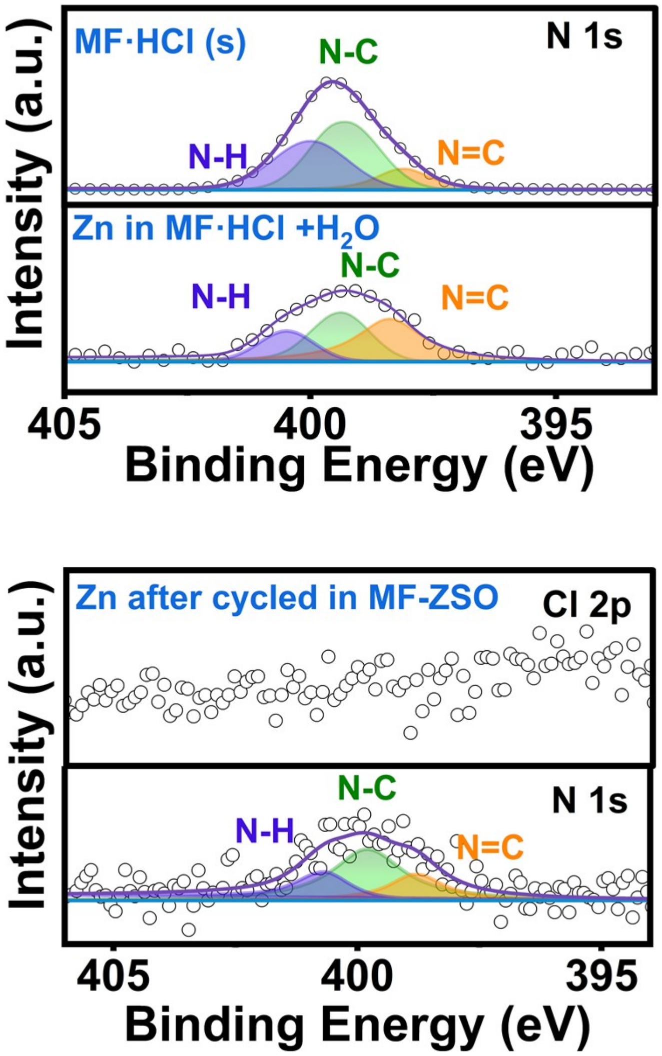

Figure S13. N spectrum of Zn immersed in MF·HCl/H_2O electrolyte (top). Cl spectrum and N spectrum of Zn foil in MF·HCl-contained electrolyte after 50 cycles at 1 mA cm^{-2} and 1 mA h cm^{-2} (below).

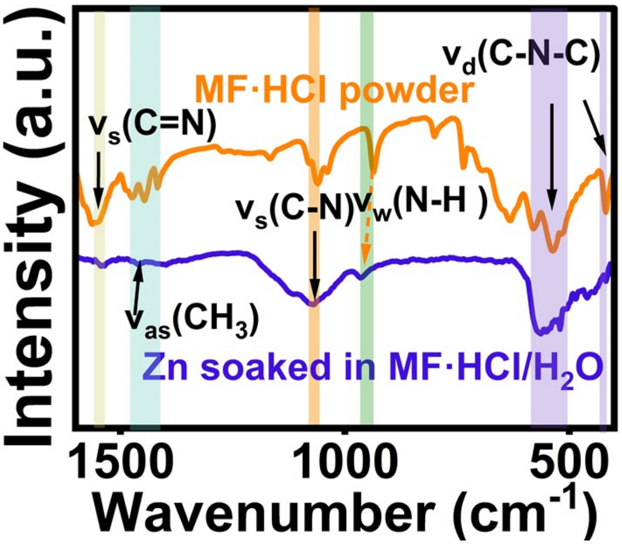

Figure S14. The FTIR peak of MF·HCl powder and Zn immersed in MF·HCl/H_2O electrolyte.

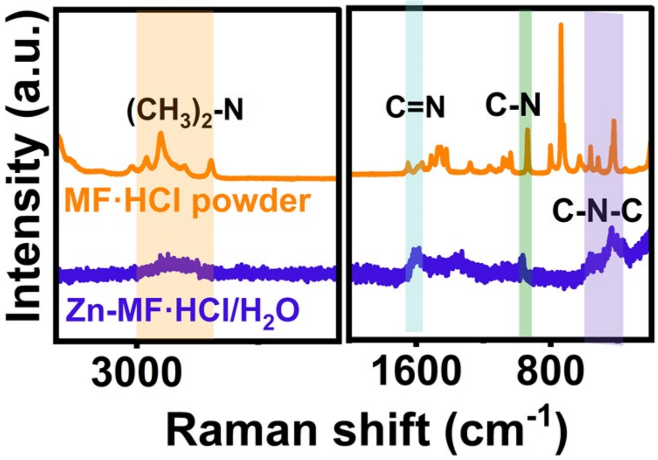

Figure S15. The Raman peak of MF·HCl powder and Zn surface immersed in MF·HCl aqueous solution (after cleaning)

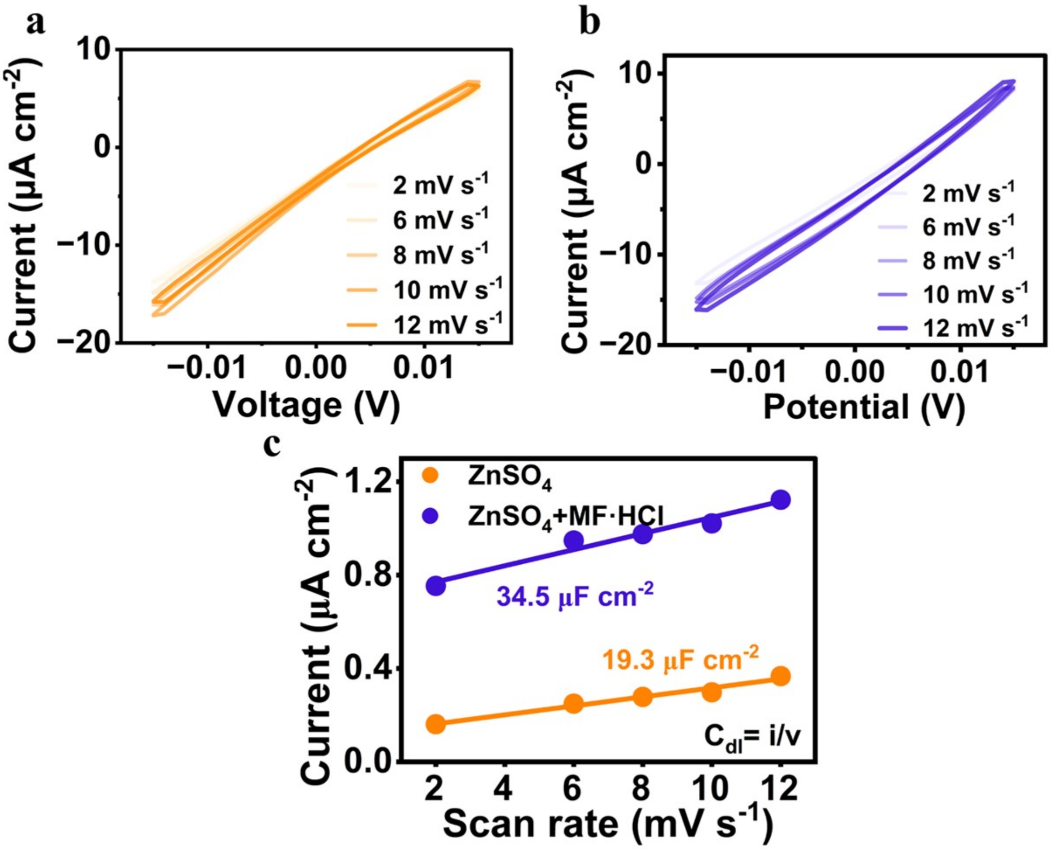

Figure S16. EDL measurement for Zn substrates in pure $ZnSO_4$ and MF·HCl electrolyte. (a) CV curves of symmetrical cells in $ZnSO_4$ solution at a voltage range of -15 to 15 mV under various scanning rates. (b) CV plot in $ZnSO_4$+MF·HCl electrolyte at the same conditions. (c) Corresponding plots of capacitive currents versus scan rates. (d) Comparisons of capacitance for two electrolyte system.

The capacitance (C) is determined by the linear relationship between capacitive current (i_c) and scan rate (v), which can be obtained from the slope of the i_c versus v graphs. Therefore, the EDL capacitance is calculated through the following equation:

$$C = \frac{i_0}{v}$$

Where i_0 refers to the capacitive currents in CV scans. Here, we define $i_0 = (i_{0v+} - i_{0v-})/2$, reflecting the half value of the current difference during a forward and negative scan at 0 V. v refers to the scan rates of 2, 6, 8, 10, 12 mV s^{-1}.

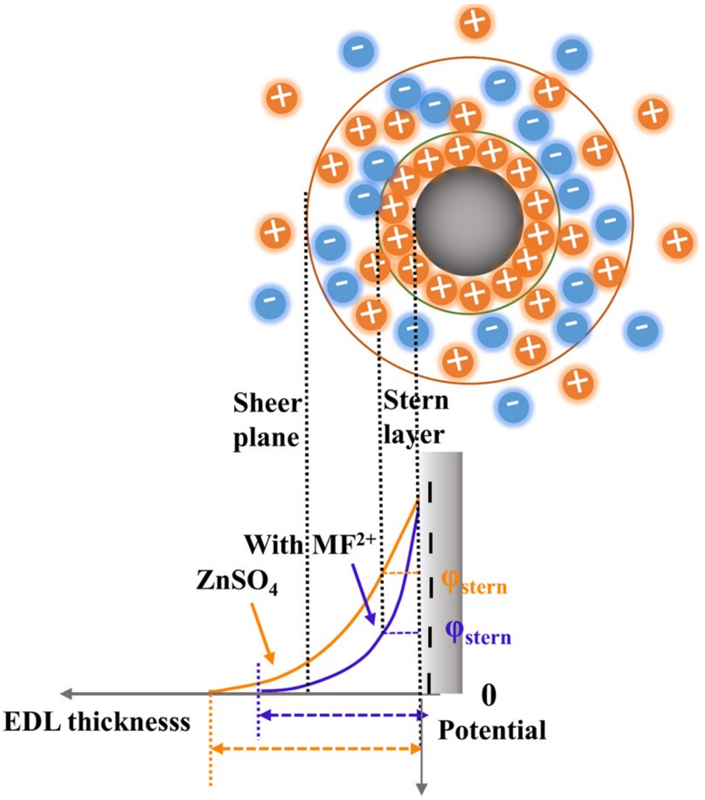

Figure S17. The structure and potential distribution of $ZnSO_4$ and EDL with MF^{2+}. The schematic shows that the EDL thickness decreases significantly after the addition of MF^{2+}, which is achieved by changing the charge structure and potential of the charged electrode surface. The addition of the additive effectively localizes the charge near the surface, thus forming a compressed surface charge layer.

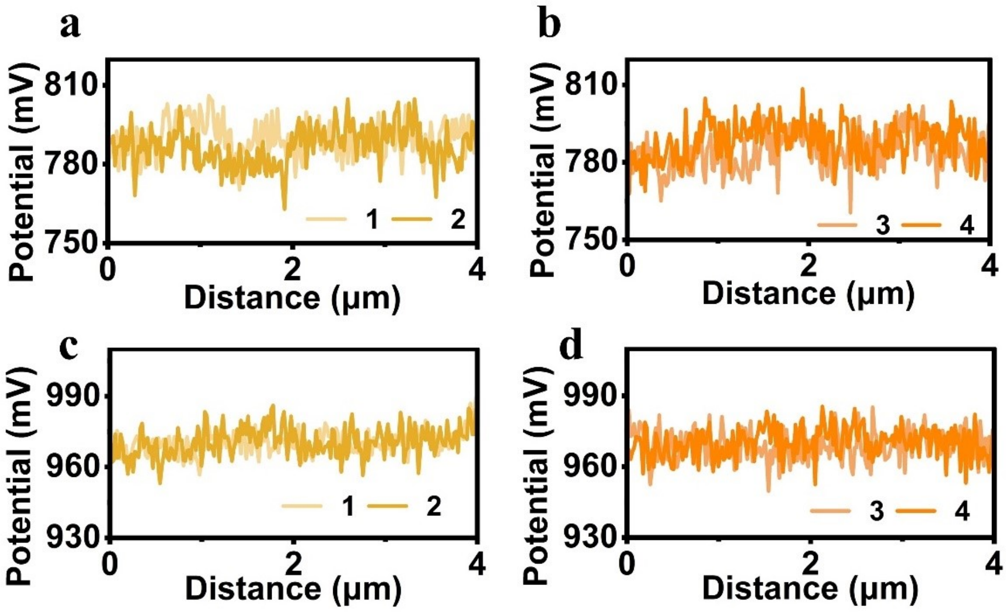

Figure S18. Line distribution of Zn surface potential in $ZnSO_4$ (a, b) and surface potential distribution of (c, d) mediated by MF・HCl.

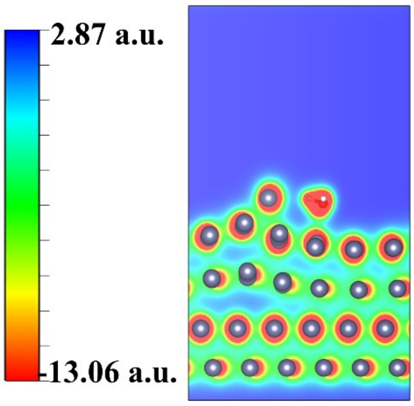

Figure S19. Electrostatic potential profile on the (1, 10, 0) plane of the H_2O-Zn(002) slab (after H_2O adsorption).

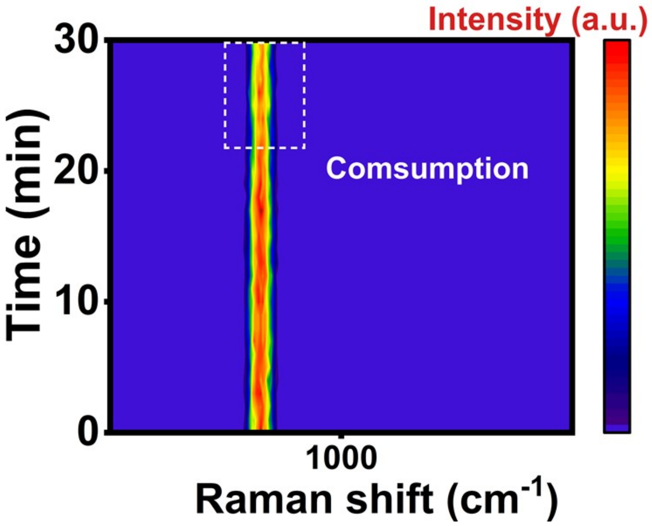

Figure S20. In situ Raman spectrum of SO_4^{2-} stretching peak in $ZnSO_4$ electrolyte.

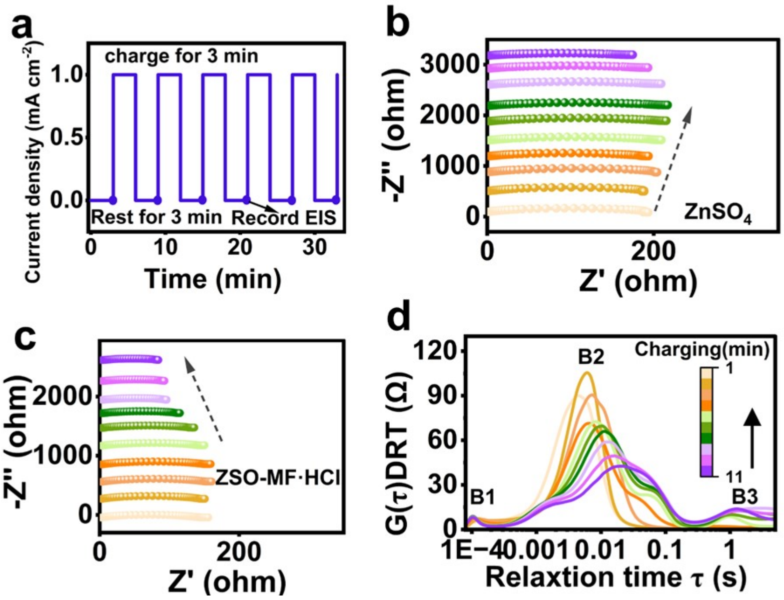

Figure S21. (a) The record method of in-situ EIS. (b) In-situ EIS during deposition of the $ZnSO_4$ and (c) $ZnSO_4$-MF • HCl electrolyte at 1 mA cm^{-2}. (d) DRT analysis of ZnSO4 during charging process. During the deposition process, the diffusion impedances (B3) of the $ZnSO_4$ electrolyte exhibit a gradual increase, while the corresponding R_{ct} (B2) initially rises before subsequently decreasing.

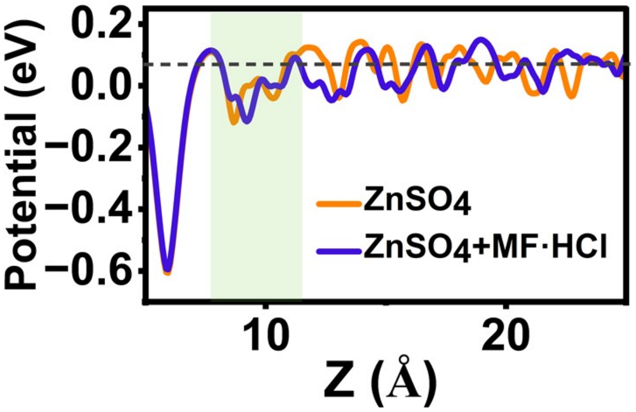

Figure S22. The electrostatic potential of with different electrolytes.

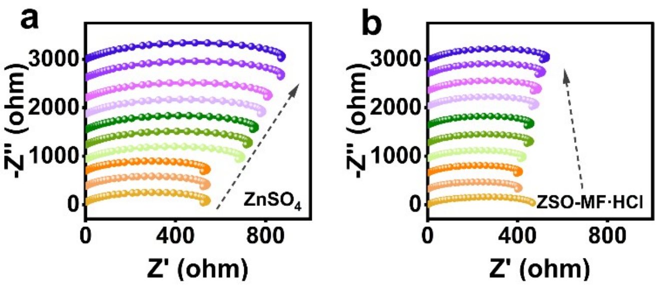

Figure S23. (a) The in-situ EIS of $ZnSO_4$ electrolyte and (b) $ZnSO_4$/MF・HCl during resting. The EIS is recorded every three minutes to measure the stability of the interface and the ease of charge transfer.

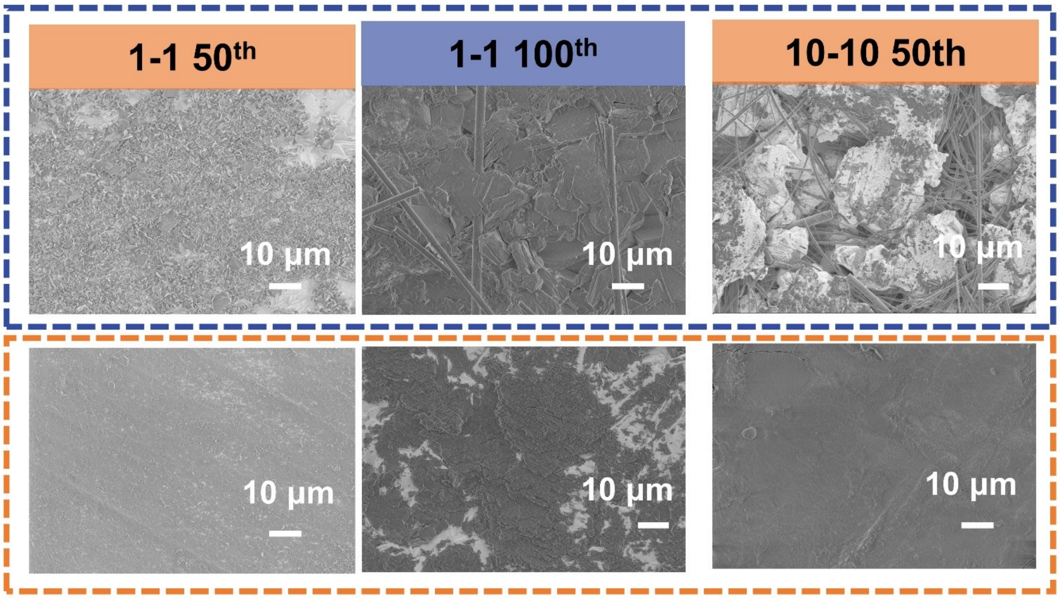

Figure S24. SEM images of Zn anodes cycled in $ZnSO_4$ (upper) and with MF·HCl additive electrolyte (below) after different cycles at 1 mA cm^{-2} with the cycling capacity of 1 mAh cm^{-2}.

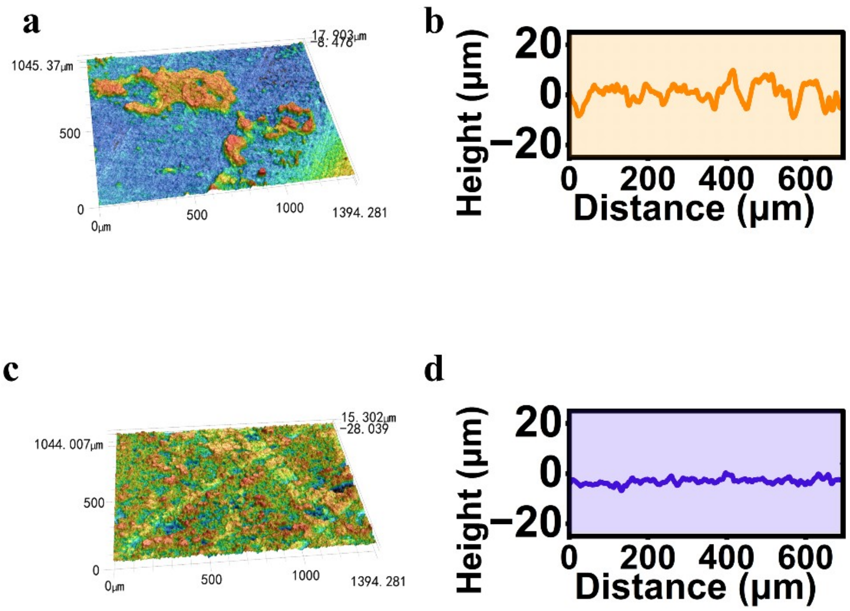

Figure S25. The corresponding optics image (a) of the anode cycled in $ZnSO_4$ electrolyte and (b) NAC-contained electrolyte under 1 mA cm^{-2} and 1 mA h cm^{-2} after 50 cycles. The height simulation diagram (c) of cycled Zn anodes in $ZnSO_4$ electrolyte and (d) MF·HCl electrolyte.

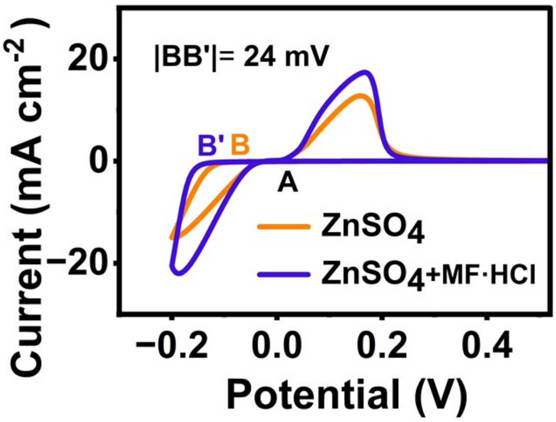

Figure S26. Voltage profile of asymmetrical cell on Ti substate in pure $ZnSO_4$ and MF·HCl electrolyte.

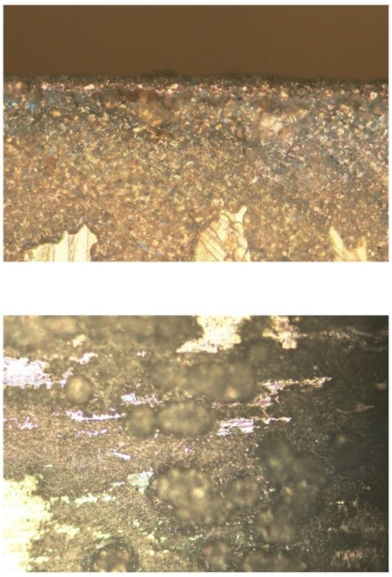

Figure S27. In situ optical microscope images of plating process for 1h in $ZnSO_4$ electrolyte (lower) and with MF·HCl electrolyte (upper) at 10 mA cm^{-2} condition.

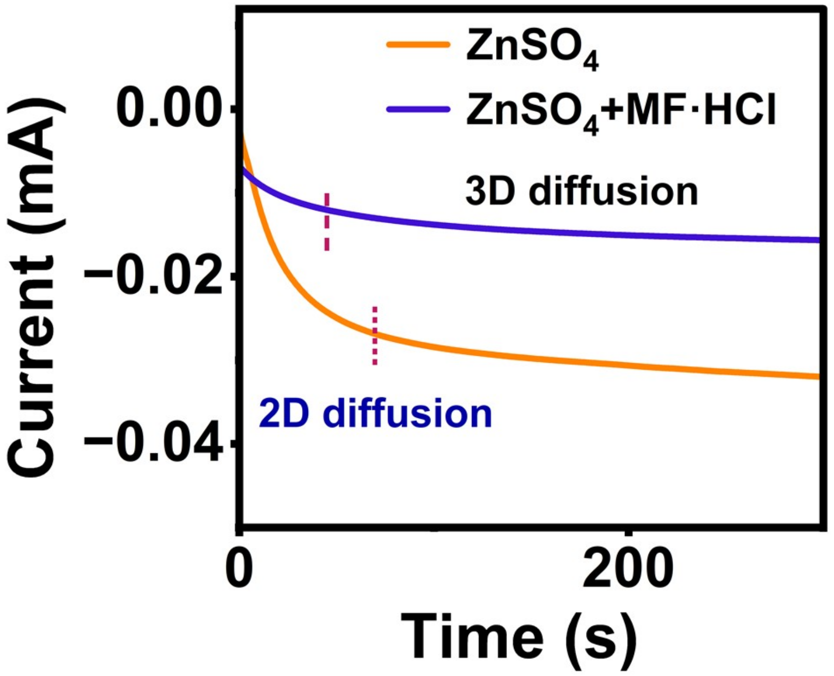

Figure S28. CA profile of atomic diffusion on the interface in pure $ZnSO_4$ and MF·HCl electrolyte.

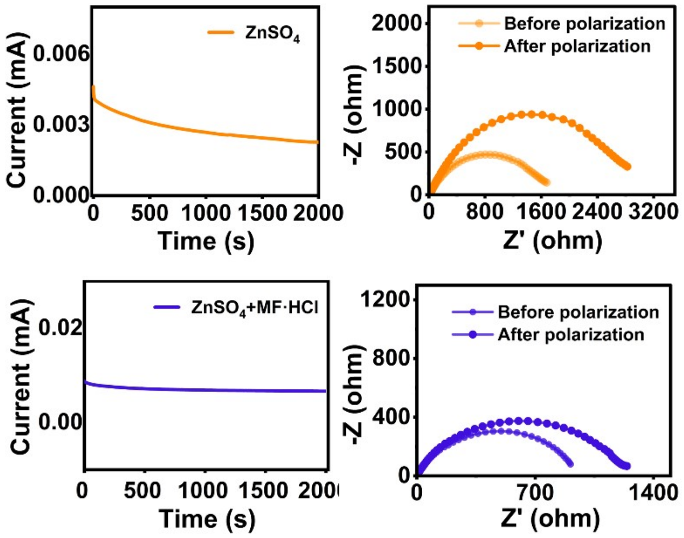

Figure S29. The current-time plots of Zn symmetric cells using (a) $ZnSO_4$ and (c) with MF·HCl after polarization at a constant potential (10 mV) for 2000 s, and the corresponding impedance spectra of (b) $ZnSO_4$ and (d) with MF·HCl before and after polarization. (e) The calculated transfer number of two system. The transference number of Zn^{2+} ($t_{Zn^{2+}}$) was evaluated by the following equation:

$$t_{Zn^{2+}} = \frac{I_S(\Delta V - I_0 R_0)}{I_0(\Delta V - I_S R_S)}$$

Where ΔV is the constant polarization voltage applied (10 mV here), I_0 (0.00464 mA, 0.00878 mA here) and R_0 (1674Ω, 908 Ω here) are the initial current and resistance, and I_S (0.00226 mA, 0.00665 mA here) and R_S (2754 Ω, 1242 Ω here) are the steady-state current and resistance, respectively.

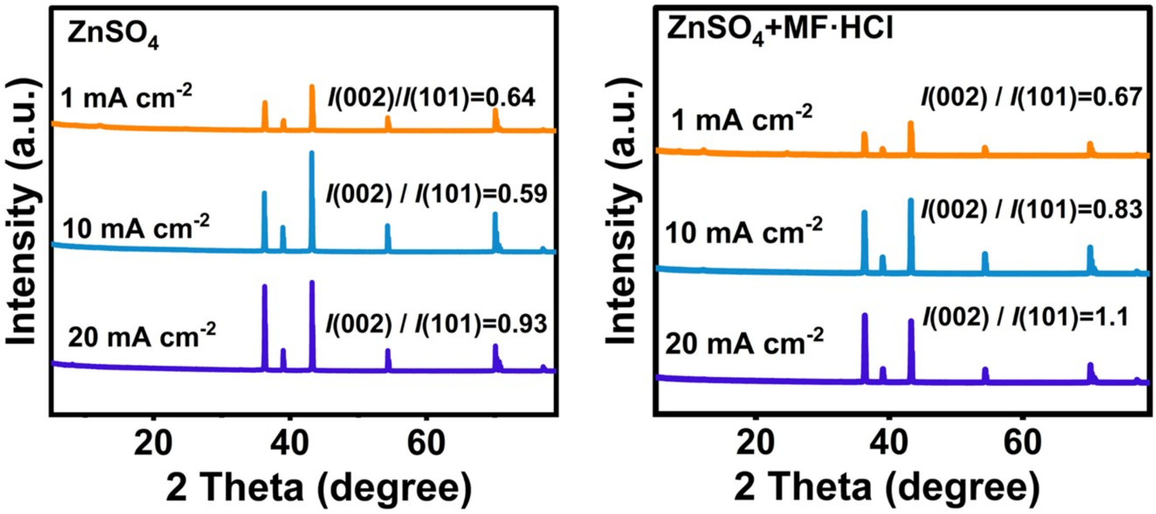

Figure S30. Texture coefficients cycling after 50 cycles at different current densities in ZSO electrolyte (left) and ZSO-MF·HCl (right).

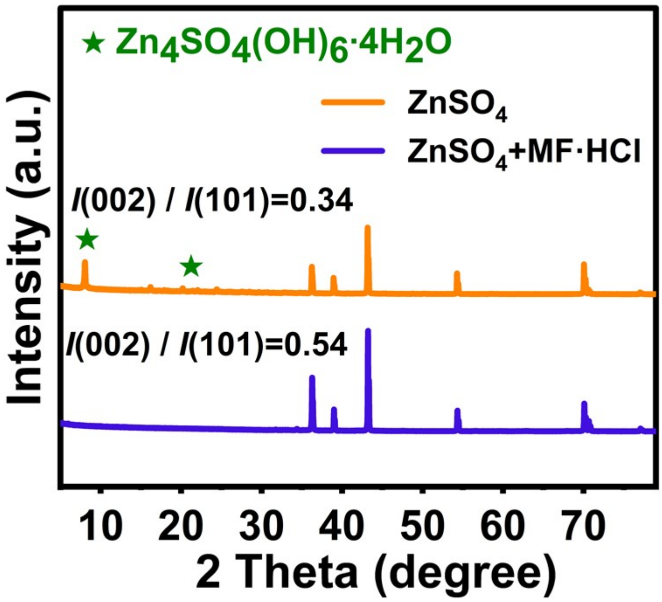

Figure S31. XRD pattern of Zn anodes in $ZnSO_4$ and $ZnSO_4$+ electrolytes after 50 cycles at 10 mA cm^{-2} and 10 mA h cm^{-2} condition.

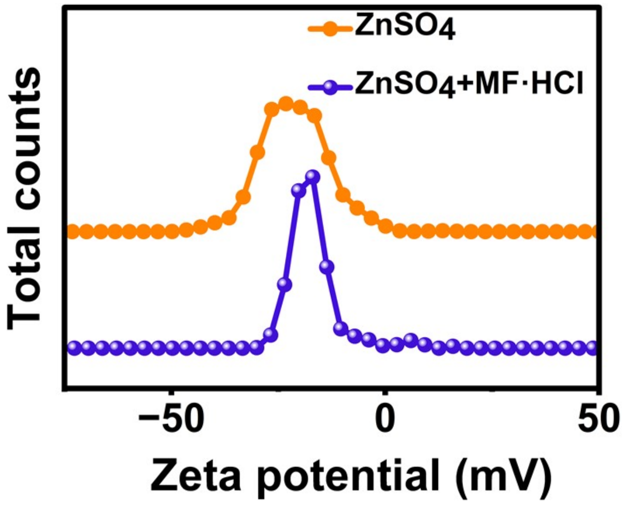

Figure S32. Zeta potential of zinc particles deposited on Ti in two electrolytes.

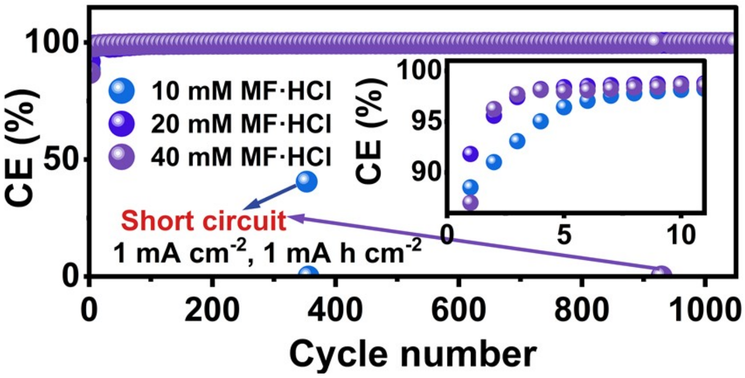

Figure S33. Comparison of Coulomb efficiency of MF·HCl containing different concentrations at 1 mA cm^{-2} and 1 mAh cm^{-2}

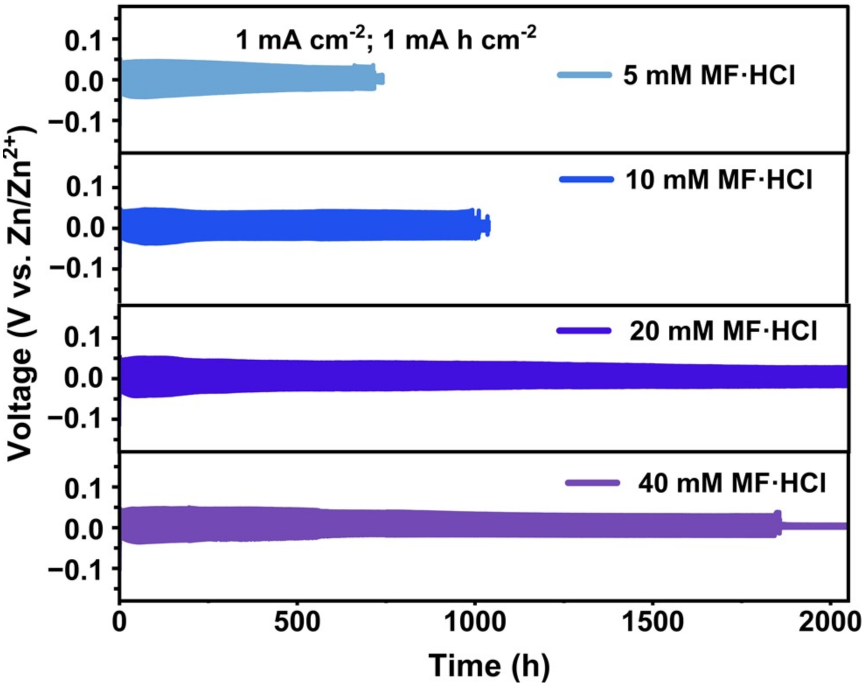

Figure S34. Cycling comparison of symmetrical cells with different amounts of MF·HCl addictive at 1 mA cm^{-2} and 1 mAh cm^{-2}. The result show that 20 mM is the optimal concentration for the most dominant effect in improving cyclic lifespan. low concentration of MF·HCl has limited effect on improving the cycling stability of Zn anode, while higher concentrations of MF·HCl may result in the formation of passivation layers due to high pH.

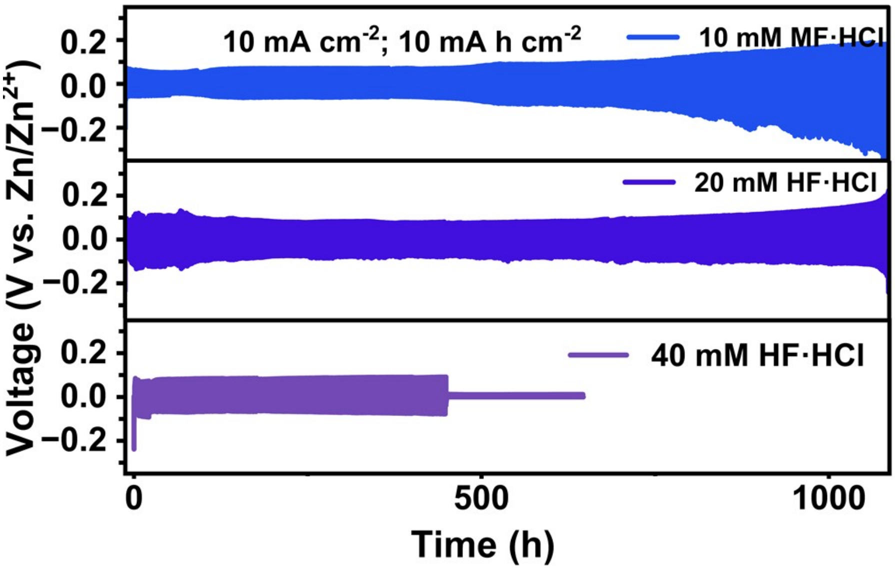

Figure S35. Cycling performance of symmetrical cells with different concentrations of MF·HCl addictive at 10 mA cm^{-2} and 10 mAh cm^{-2}

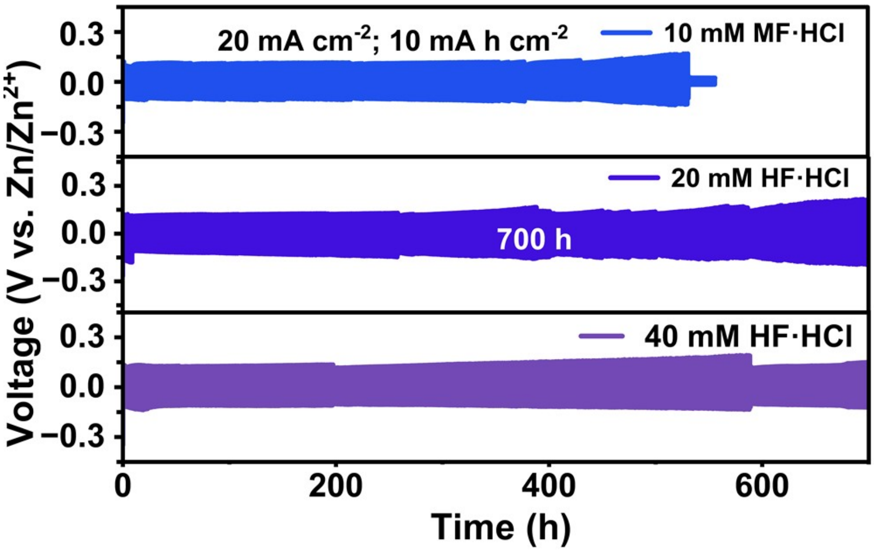

Figure S36. Cycling performance of symmetrical cells with different concentrations of MF·HCL addictive at 20 mA cm^{-2} and 10 mAh cm^{-2}

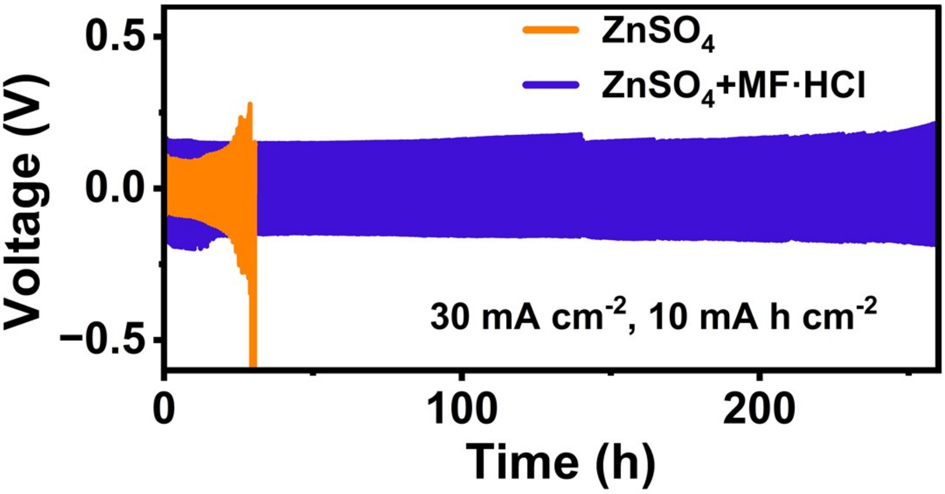

Figure S37. Long-term galvanostatic cycling of symmetric cells employing $ZnSO_4$, $ZnSO_4$+MF·HCl at a current density of 30 mA cm^{-2} and areal capacity of 10mA h cm^{-2}

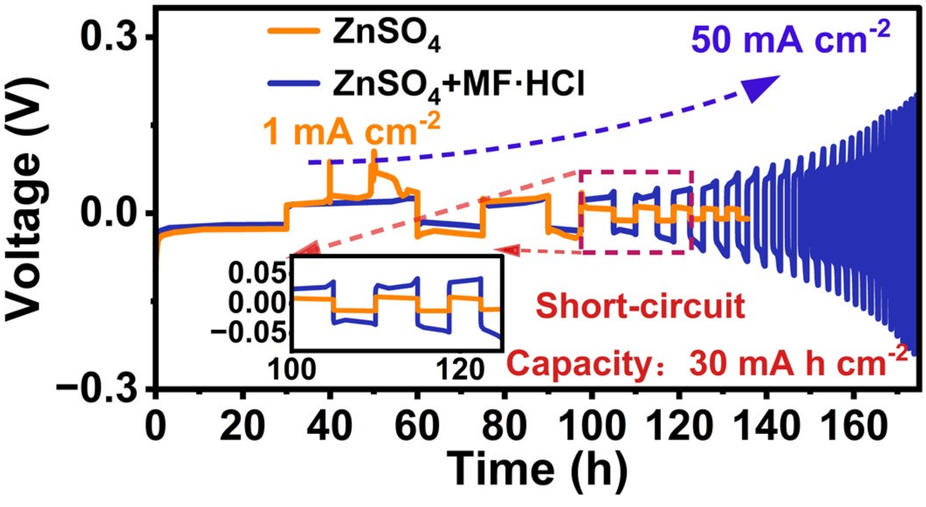

Figure S38. The limiting current density of two kinds of electrolyte is tested under constant capacity condition with increasing current density from small to large

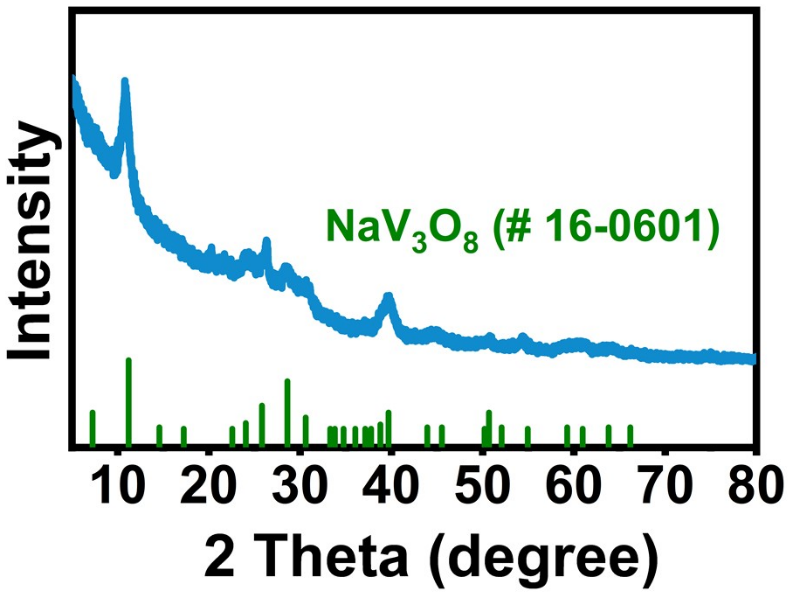

Figure S39. XRD pattern of prepared NaV3O8 powders.

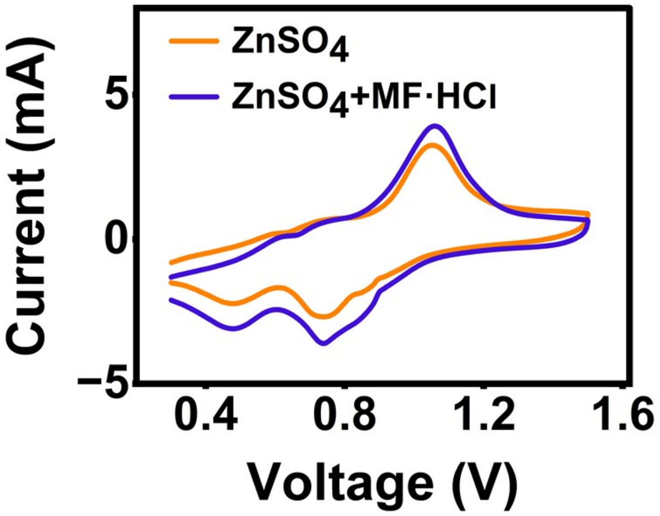

Figure S40. CV curves of Zn Zn||NVO full cells for the first cycle.

Table S1: Comparison of different reported EDL-tuning strategies.

Additive	Strategies	Scientific significance	Unsolved problems	Ref.
La^{3+}	Electrostatic repulsion decreases - Debye length decreases	First discuss weaken EDL repulsive force to favor dense deposits	No concern about the effect of compressed EDL on ion charge distributions	12
SDE	Sieving-type EDL by hydrogen bond interlock	Sieving-type EDL to achieve dendrite-free anode	Ignore the potential dependence of EDL No high current performance	13
NAC	Proton-mediated transformation between solvation structure and interfacial adsorption	Proton- mediated dynamic molecular transformation to achieve dendrite-free and corrosion-free Zn anodes	No attention to the analysis of charge properties as cations and the lack of interfacial diffusion behavior	14
APM	H_2O-poor EDL	Dead Zn is caused by the solvation of Zn^{2+} and H_2O	No direct evidence for the formation of H_2O-poor EDL	15
NCAP	Zincophilic H_2O-poor EDL	Negative charged acidic polarity to reconstruct solvation structure or adsorption on EDL regulation	The dependence of EDL on potential and the relationship between electron transfer and atomic self-diffusion are not considered	16
TMA	Regulate interfacial chemistry	Mediating the $Zn(H_2O)_6^{2+}$ structure at the interface and strong resistance against corrosion	No concern about the effect of additive in EDL	17
This work	Transfer-mediated EDL compression	Compressing EDL by mediating the interaction of ionic charges near the charged interface, and shorten the transport path of Zn^{2+} Redistribute the electron distribution on the metal surface and balance the relationship between electron transfer and zinc atom diffusion.	—	—

Table S2: The charge transfer impedance and error rate of in-situ EIS during charging fitted by ZView software.

Point	Rct in $ZnSO_4$	Error%	T-CPE	Rct in $ZnSO_4$+MF·HCl	Error%	T-CPE
1	194.0	0.76	5.8E-5	141.0	0.46	8.3E-5
2	197.5	1.41	8.7E-5	145.7	0.45	1.1E-4
3	213.4	1.50	1.2E-4	154.6	0.88	1.4E-4
4	192.3	0.70	1.4E-4	154.3	1.12	1.8E-4
5	207.3	1.12	1.6E-4	149.3	1.57	2.6E-4
6	213.5	0.45	2.0E-4	131.6	0.69	2.9E-4
7	213.2	0.51	2.3E-4	120.2	2.62	5.4E-4
8	204.9	0.68	2.8E-4	97.11	1.27	5.7E-4
9	192.6	0.91	3.6E-4	89.6	2.05	9.5E-4
10	176.0	1.16	4.8E-4	82.8	1.08	8.3E-4

Reference

1. M. J. Abraham, T. Murtola, R. Schulz, S. Páll, J. C. Smith, B. Hess and E. Lindahl, *SoftwareX*, 2015, **1-2**, 19-25.
2. D. S. M. William L. Jorgensen, and Julian Tirado-Rives, *J. Am. Chem. Soc*, 1996, **118**, 11225-11236.
3. G. Kresse and J. Furthmüller, *Physical Review B*, 1996, **54**, 11169-11186.
4. J. P. Perdew, K. Burke and M. Ernzerhof, *Phys. Rev. Lett.*, 1996, **77**, 3865-3868.
5. G. Kresse and D. Joubert, *Physical Review B*, 1999, **59**, 1758-1775.
6. P. E. Blöchl, *Physical Review B*, 1994, **50**, 17953-17979.
7. S. Grimme, J. Antony, S. Ehrlich and H. Krieg, *The Journal of Chemical Physics*, 2010, **132**.
8. J. Hutter, M. Iannuzzi, F. Schiffmann and J. VandeVondele, 2014, **4**, 15-25.
9. J. VandeVondele and J. Hutter, *The Journal of Chemical Physics*, 2007, **127**.
10. S. Goedecker, M. Teter and J. Hutter, *Physical Review B*, 1996, **54**, 1703-1710.
11. S. Nosé, *The Journal of Chemical Physics*, 1984, **81**, 511-519.
12. R. Zhao, H. Wang, H. Du, Y. Yang, Z. Gao, L. Qie and Y. Huang, *Nat Commun*, 2022, **13**, 3252.
13. T. Yan, B. Wu, S. Liu, M. Tao, J. Liang, M. Li, C. Xiang, Z. Cui, L. Du, Z. Liang and H. Song, *Angew. Chem. Int. Ed.*, 2024, **63**, e202411470.
14. S. Zheng, K. Zhang, B. Luo, L. Sun, Z. Bao, G. Duan, J. Huang, Z. Gu, Z. Ye and Y. Wang, *Energy Storage Mater*, 2024, **71**.
15. K. Qi, P. Liang, S. Wei, H. Ao, X. Ding, S. Chen, Z. Fan, C. Wang, L. Song, X. Wu, C. Wu and Y. Zhu, *Energy Environ. Sci.*, 2024, **17**, 2566-2575.
16. X. Fan, L. Chen, Y. Wang, X. Xu, X. Jiao, P. Zhou, Y. Liu, Z. Song and J. Zhou, *Nanomicro Lett*, 2024, **16**, 270.

17 L. Zheng, H. Li, M. Gao, K. Huang, J. Wang, L. Su, L. Li, H. Lin, X. Gao, Z. Liu and H. Zhang, *Advanced Science*, 2024, **11**, e2407102.